SUPPORTING INFORMATION

Controlled Living Nanowire Growth: Precise Control over the Morphology and Optical Properties of AgAuAg Bimetallic Nanowires

Martin Mayer,[a,§] Leonardo Scarabelli,[b,§] Katia March,[c] Thomas Altantzis,[d] Moritz Tebbe,[a] Mathieu Kociak,[c] Sara Bals,[d] F. Javier García de Abajo,[e,f] Andreas Fery,[a] Luis M. Liz-Marzán[b,g,*]

[a]*Physical Chemistry II, University of Bayreuth, Universitätsstraße 30, 95440 Bayreuth, Germany*

[b]*CIC biomaGUNE, Paseo de Miramón 182, 20009 Donostia - San Sebastián, Spain*

[c]*Laboratoire de Physique des Solides CNRS/UMR8502, Bâtiment 510, University Paris-Sud, Orsay 91405, France*

[d]*EMAT, University of Antwerp, Groenenborgerlaan 171, 2020 Antwerp, Belgium*

[e]*ICFO-Institut de Ciencies Fotoniques, Mediterranean Technology Park, 08860 Castelldefels (Barcelona), Spain*

[f]*ICREA-Institució Catalana de Recerca i Estudis Avançats, Passeig Lluís Companys, 23, 08010 Barcelona, Spain*

[g]*Ikerbasque, Basque Foundation for Science, 48013 Bilbao, Spain*

[§]Martin Mayer and Leonardo Scarabelli contributed equally

*Corresponding author's e-mail: llizmarzan@cicbiomagune.es

1. Nanorod-Purification

Since the presence of byproducts (NPs with different shapes) ultimately limits the use of PT-AuNRs as seeds for silver overgrowth, a purification step was required to separate nanorods from other NPs. Shape-dependent separation can be achieved by exploiting depletion interaction forces.[1–4] A depletion force is an effective attractive force that arises between large colloidal particles that are suspended in a dilute solution of depletants, which are smaller solutes that are preferentially excluded from the vicinity of the large particles[5]. In our case the depletants are CTAC micelles and the depletion force can be modulated according to the following equation:

$$|U| = \frac{2 \cdot r_m \cdot A \cdot N_{AV} \cdot (C - C_{cmc})}{AN} k_B T$$

where r_m, C_{cmc}, C and AN are respectively the radius, the critical micellar concentration, the analytical concentration and the aggregation number of the chosen surfactant, N_{AV} is Avogadro's number, and A is the area of interaction between two adjacent particles. The choice of CTAC arises from its high water solubility compared to CTAB or BDAC; since CTAC only varies from CTAB in the counter-ion, the surfactant used for PT-AuNR synthesis, and considering that it is present with a concentration as low as 8 mM, no washing is required prior to surfactant exchange, *i.e.* the required CTAC amount was added directly to the PT-AuNR solution. To obtain the highest possible purification degree, different surfactant concentrations between 0.05 M and 0.15 M were screened for each PT-AuNR batch. To calculate the amount of CTAC stock solution needed to reach a desired final concentration it is enough to solve the following equation:

$$V_x = \frac{V_{in}(C_{fin} - C_{in})}{C_{stock} - C_{fin}}$$

Where V_x is the volume of CTAC stock solution (of concentration C_{stock}) needed to reach the desired final concentration C_{fin} from a solution of nanoparticles with an initial volume V_{in} and an initial concentration C_{in}. We assume that the initial concentration was that of CTAB: even though CTAB and CTAC present

different cmc values, we consider this an acceptable simplification considering the low concentration of CTAB used for the PT-AuNR growth. After screening different [CTAC], a concentration around 0.1 M was found to lead to selective flocculation and precipitation of PT-AuNRs within 12 hours (Figure S1).
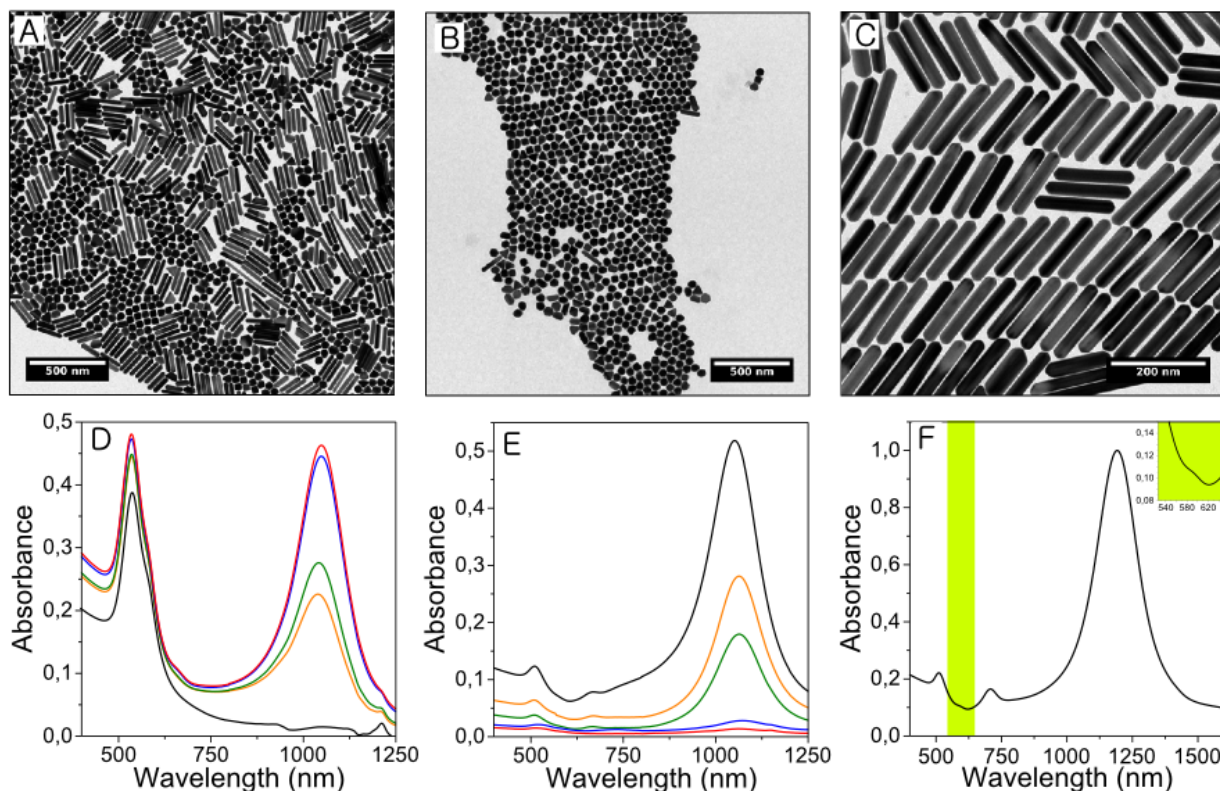

Figure S1. Purified PT-AuNR solution used as core for controlled living nanowire growth. A: TEM image of as-synthesized PT-AuNRs. **B:** TEM image from the supernatant containing the synthesis by-product. **C:** TEM image of purified PT-AuNRs. **D:** UV-Vis analysis of the supernatant obtained 16 hours after addition of CTAC solutions; [CTAC]=0.12M (black curve), 0.10M (orange curve), 0.08M (green curve), 0.06M (blue curve) and 0.04M (red curve). **E:** UV-Vis analysis of the precipitate obtained 16 hours after the addition of CTAC stock solution. The curve colors correspond to those in D. **F:** UV-Vis spectra of a purified PT-AuNRs solution; **inset:** zoom of the highlighted area discerning the octupolar mode.
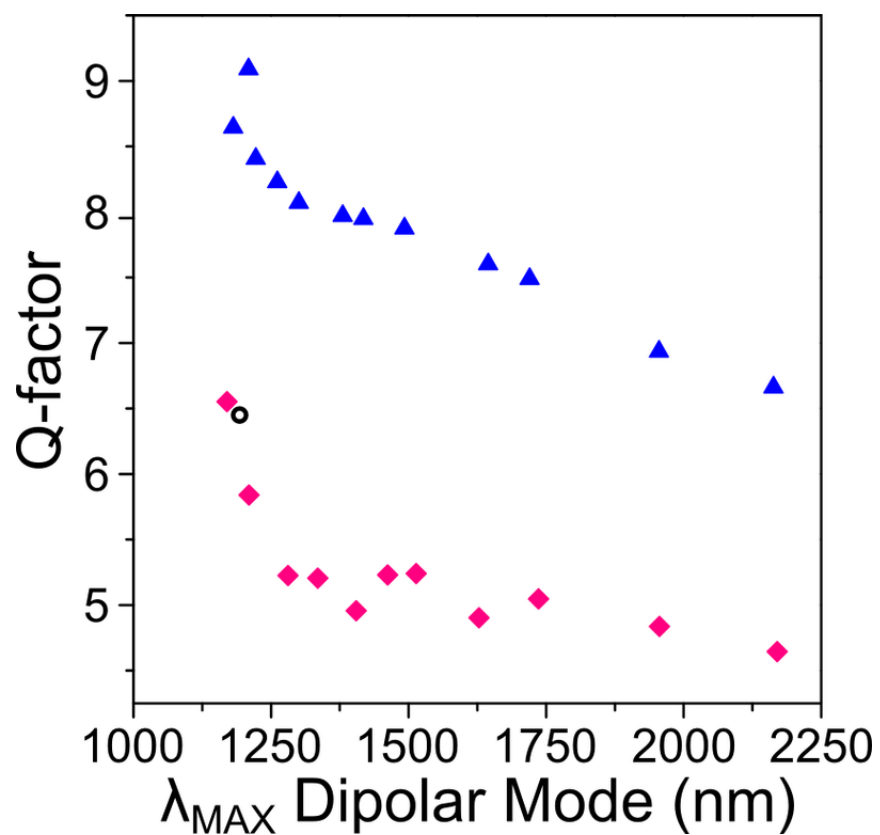
Figure S2. Evolution of the Q-factor during living nanowire growth. Experimentally (pink diamonds) we observed an exponential decrease in Q-factor as a function of the dipole mode position. This trend was confirmed by BEM calculations (blue triangles). Interestingly the theoretical values are only 25% higher and show a similar decay rate, confirming the low polydispersity of AgAuAg NWs throughout the entire reaction. The black circle is the Q-factor of the starting PT-AuNRs solution.

Table S1. Summary of the TEM analysis relative to Figure 1A. It should be noticed that the NWs thickness increases at early growth stages, but then remains constant throughout all the experiment. The last two samples (AgEn=3.82 and 8.59) are not shown in Figure 1A for clarity.

AgEn	Thickness (nm)	Length (nm)	AR	Ag length per tip (nm)	λ_{MAX} Dipole LSPR (nm)
0	34 ± 1	210 ± 10	6.1 ± 0.4	//	1192
0.24	38 ± 1	220 ± 10	5.7 ± 0.5	3 ± 1	1170
0.36	38 ± 1	230 ± 10	6.0 ± 0.4	7 ± 2	1210
0.48	38 ± 1	240 ± 10	6.3 ± 0.5	17 ± 4	1281
0.60	38 ± 1	250 ± 20	6.7 ± 0.5	24 ± 4	1335
0.72	38 ± 1	270 ± 20	7.1 ± 0.5	33 ± 6	1405
0.84	39 ± 2	280 ± 20	7.3 ± 0.7	39 ± 8	1462
0.96	37 ± 2	300 ± 20	8.1 ± 0.7	50 ± 10	1514
1.20	38 ± 1	340 ± 20	8.9 ± 0.5	61 ± 9	1628
1.44	37 ± 2	360 ± 30	9.7 ± 0.9	75 ± 9	1736
1.92	38 ± 2	420 ± 30	11 ± 1	100 ± 10	1956
2.40	37 ± 2	470 ± 40	13 ± 2	130 ± 20	2170
5.76	38 ± 2	820 ± 90	21 ± 3	300 ± 40	//*
11.52	39 ± 3	1500 ± 200	39 ± 7	660 ± 90	//*

*The dipole resonance was red-shifted beyond the detection limit of the instrument
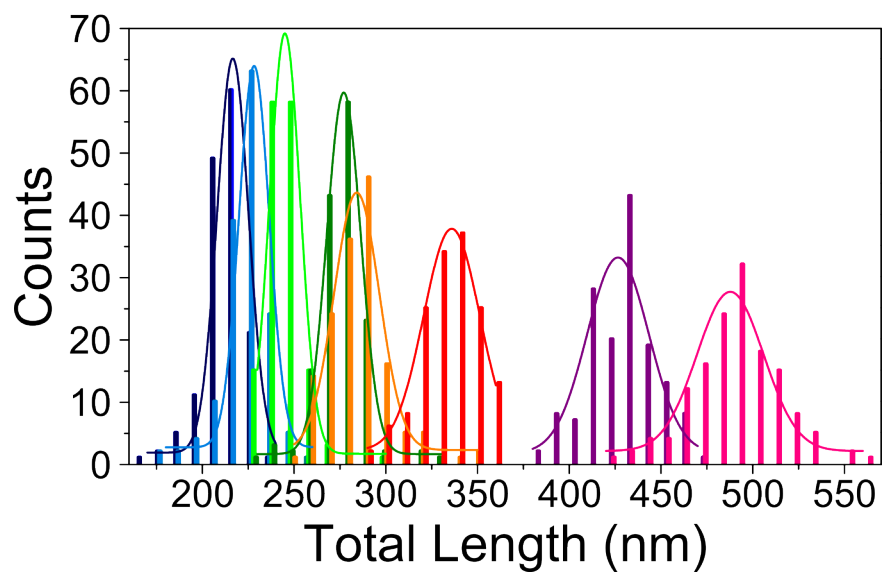
Figure S3. Total length distribution histograms of the 8 samples discussed in Figure 1A and Table S1. The colors are the same as in Figure 1A. Histograms were obtained by measuring 150 NRs for each sample.
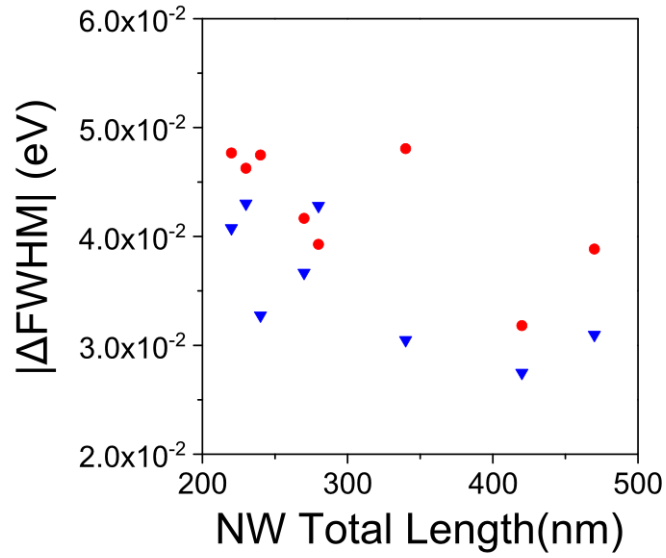
Figure S4. Increase in plasmon FWHM due to the finite size distribution of the NWs. We compare the following two quantities: (1) difference of FWHM in experiment minus theory (red circles); (2) estimate of increase in FWHM extracted from the standard deviation of NW lengths observed in TEM images, multiplied by the derivative of the plasmon energy with respect to NW length (blue triangles). We only show results for the lowest-order plasmon mode. This figure confirms that the observed (moderate) increase in FWHM of experiment compared with theory is fully attributable to the finite distribution of NW lengths.
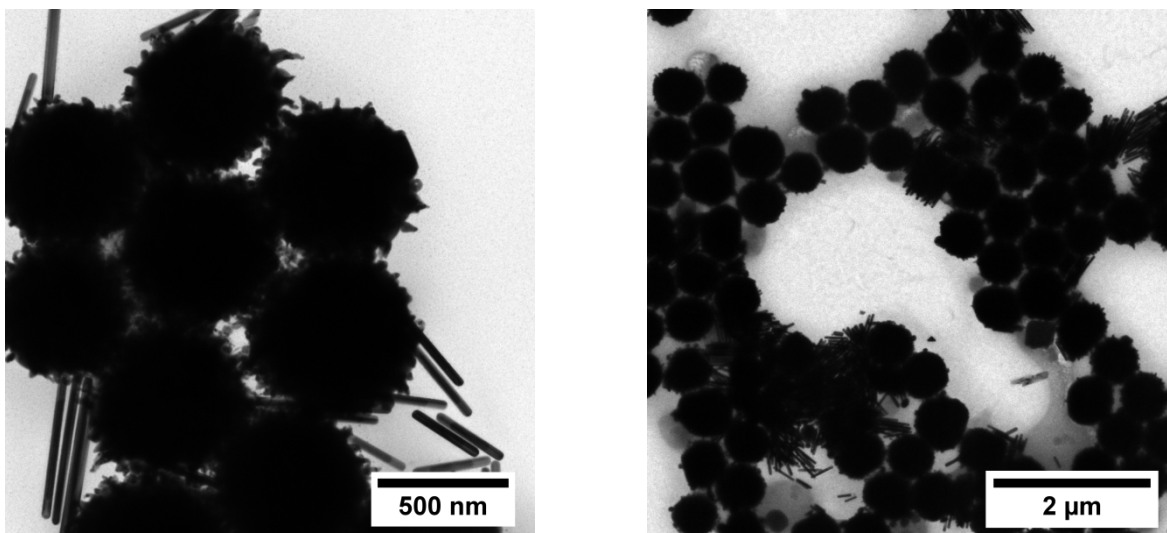
Figure S5. AgCl particles observed upon drying when a higher addition rate was used for NW synthesis. The formation of these particles is likely due to accumulation of AgCl in the growth solution.

Table S2. Summary of TEM analysis of NWs obtained using a higher addition rate (see Figure 1C). The selective deposition of silver is less efficient, as seen from a double increment of NWs thickness compared to living growth conditions (see Table S1).

AgEn	Thickness (nm)	Length (nm)	AR	Ag length per tip (nm)	λ_{MAX} Dipole LSPR (nm)
0	33.3 ± 0.9	182 ± 10	5.4 ± 0.3	//	1078
0.36	37 ± 2	193 ± 9	5.3 ± 0.4	5.1 ± 0.4	1061
0.73	38 ± 1	201 ± 11	5.3 ± 0.4	9.1 ± 0.7	1076
1.46	38 ± 2	208 ± 19	5.4 ± 0.6	13.0 ± 0.7	1143
1.84	39 ± 1	228 ± 12	5.8 ± 0.4	23 ± 2	1187
2.58	39 ± 2	266 ± 22	6.8 ± 0.6	42 ± 4	1288
3.33	40 ± 1	300 ± 19	7.6 ± 0.6	59 ± 4	1364
4.08	40 ± 1	313 ± 28	7.8 ± 0.9	65 ± 7	1468
4.84	39 ± 1	313 ± 23	8.1 ± 0.7	65 ± 6	1567
5.60	39 ± 2	362 ± 26	9.3 ± 0.9	90 ± 9	1685
6.54	39 ± 1	406 ± 23	10.5 ± 0.7	112 ± 7	1850
7.49	39 ± 1	451 ± 31	12 ± 1	134 ± 12	2036
8.26	39 ± 2	489 ± 28	13 ± 1.2	153 ± 14	2232
8.74	41 ± 2	898 ± 57	22 ± 2	358 ± 30	//*

*The dipole resonance was red-shifted beyond the detection limit of the instrument

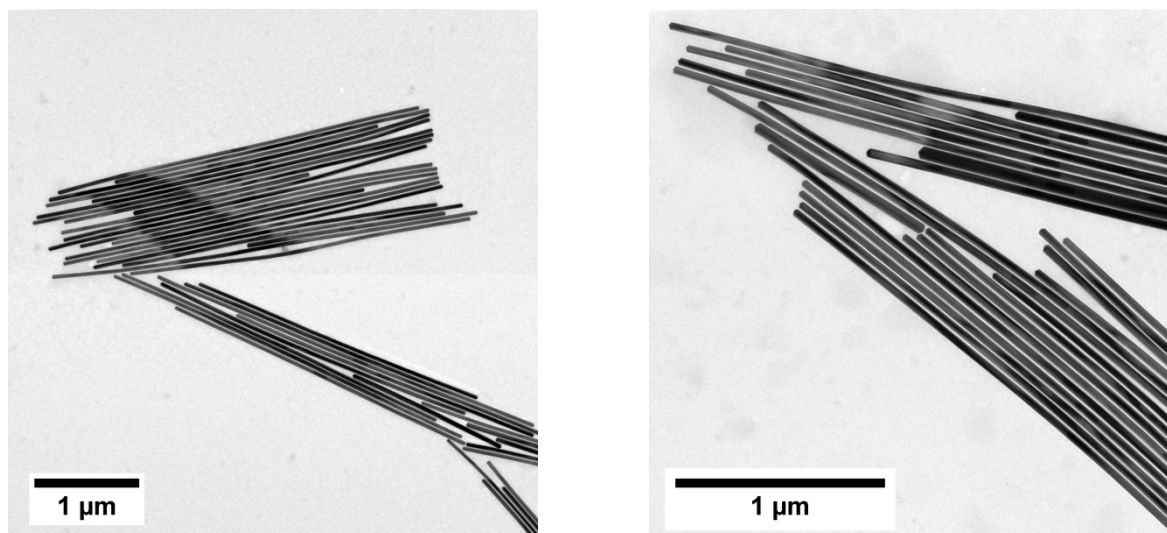**Figure S6.** TEM images of AgAuAg NWs after 7 days of growth (AgEn=40.32). The average dimensions are: 3.4 ± 0.6 µm in length, 37 ± 2 nm in thickness, corresponding to an average Ag length per tip of 1.6 ± 0.2 µm, and an aspect ratio of 90 ± 10.
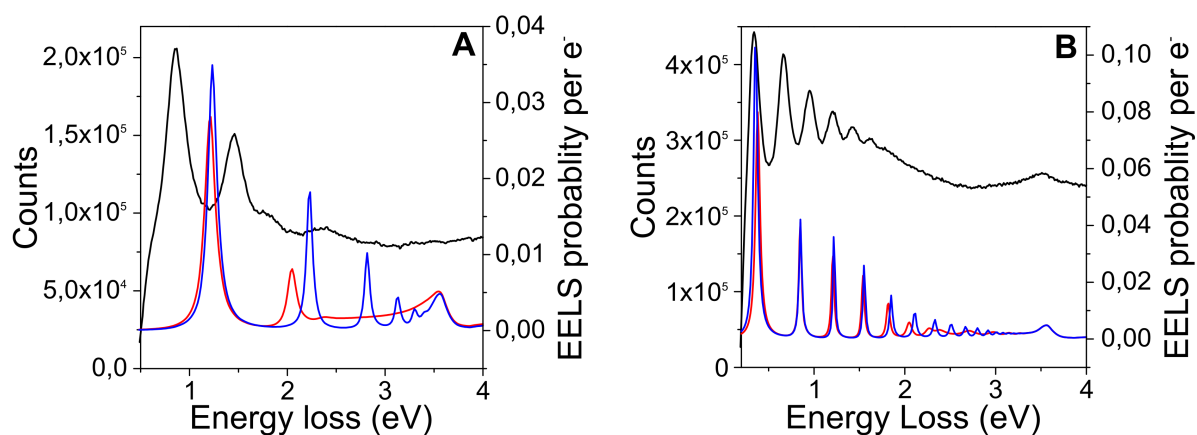

Figure S7. Experimental EELS spectra (black) and calculated spectra, in the presence (red) and absence (blue) of the gold core. The Experimental spectra were background corrected to eliminate the zero loss peak. **A:** AgEn=0.5. **B:** AgEn=5.3.
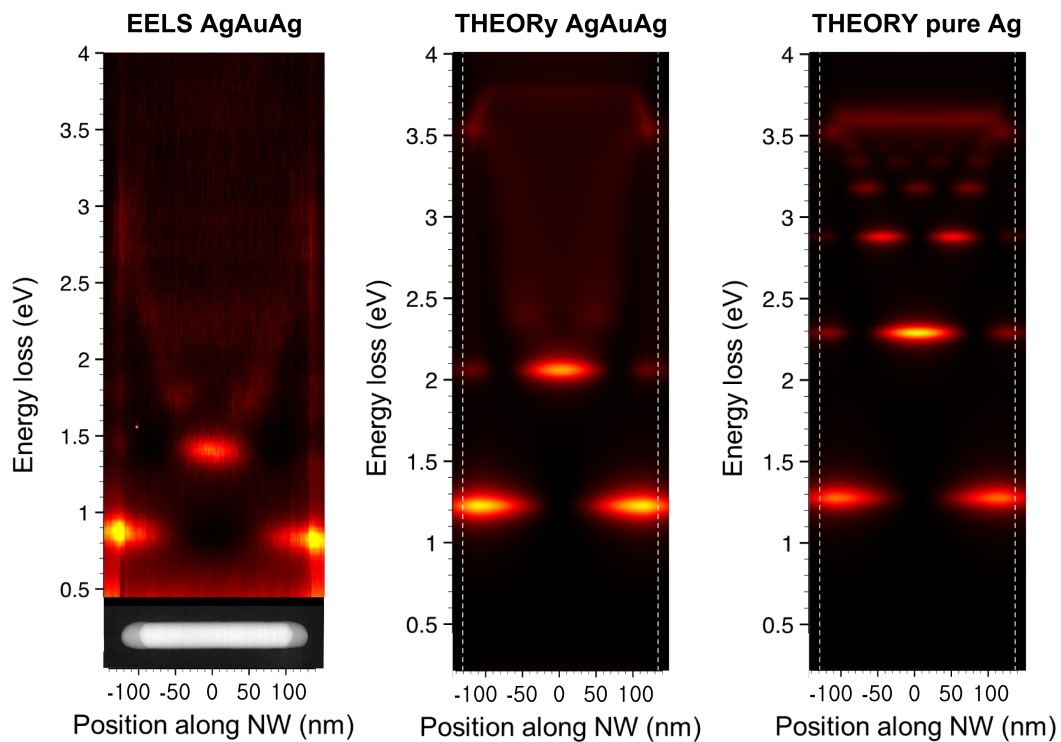
Figure S8. Experimental and calculated EELS data as a function of energy for the sample with AgEn=0.5.
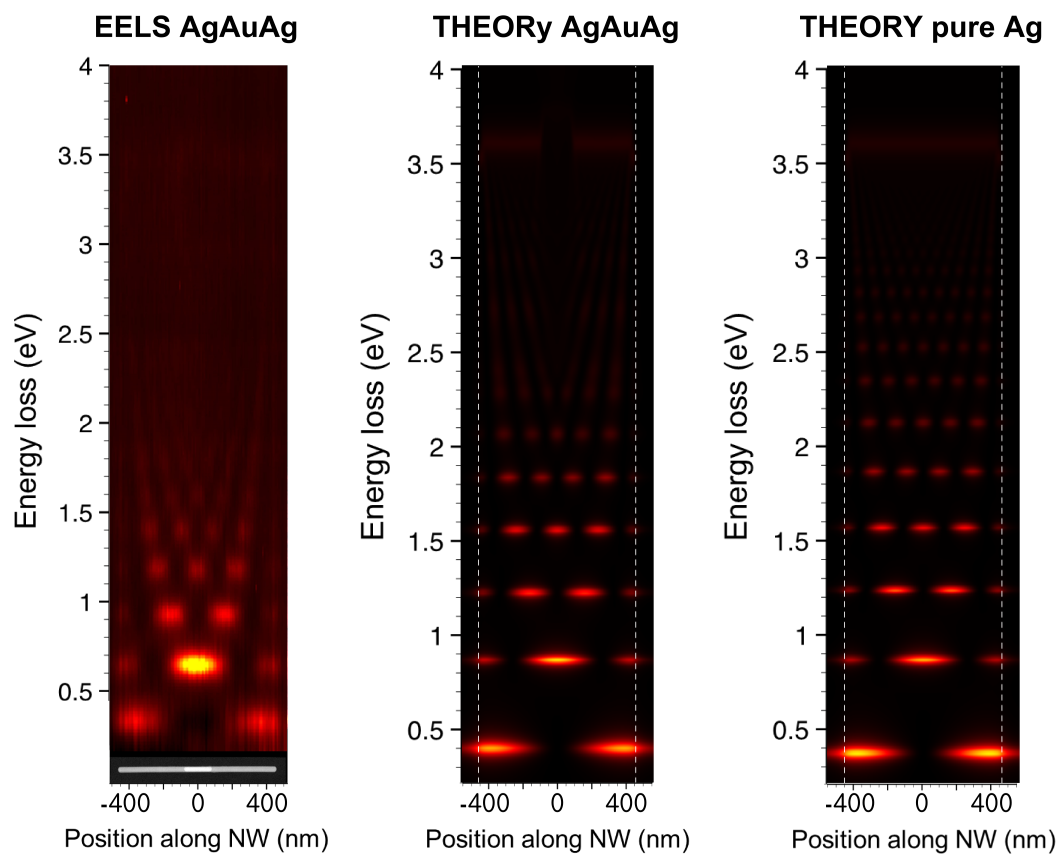
Figure S9. Experimental and calculated EELS data as a function of energy for the sample with AgEn=5.3.

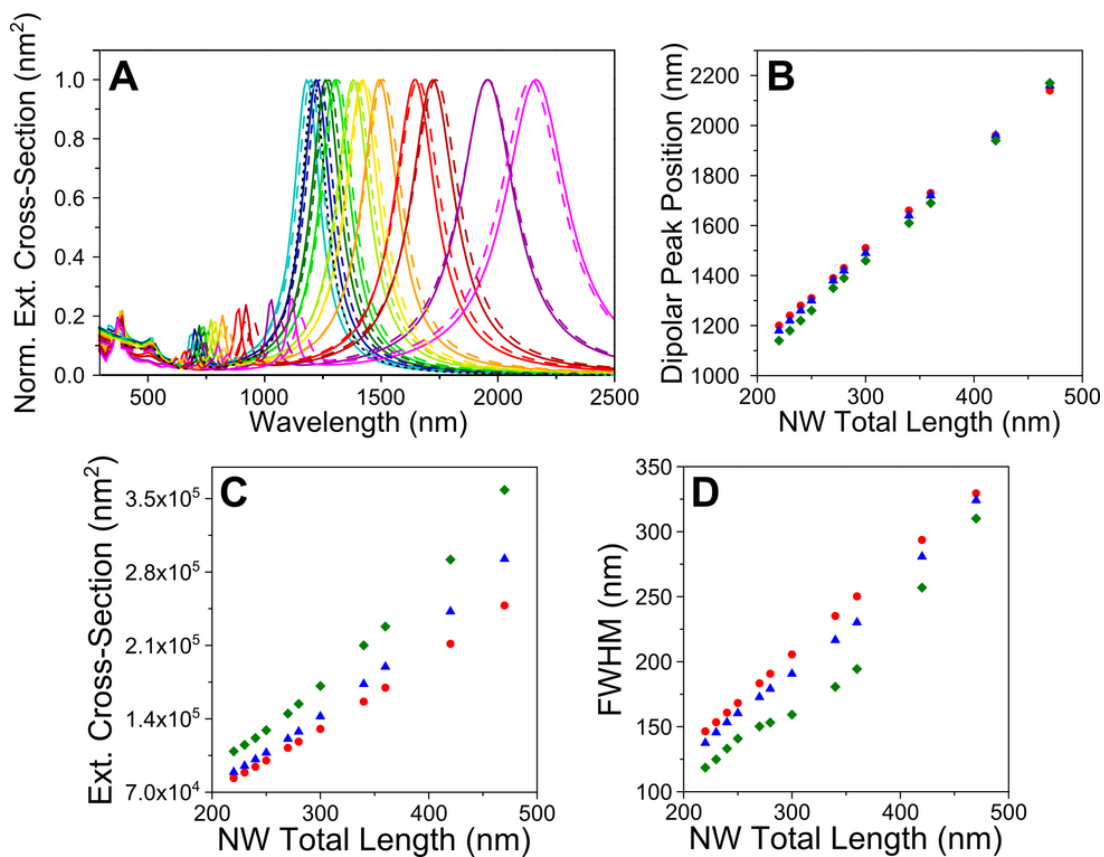**Figure S10. A:** calculated (BEM) extinction spectra of AgAuAg (solid curves) and pure Au (dashed curves) NWs with dimensions corresponding to the experimental ones (same color code used for **Figure 1A**). **B-D:** Comparison between pure Au (red circles), pure Ag (green diamonds) and bimetallic AgAuAg NWs (blue triangles) for: dipolar peak position (**B**), extinction cross-section (**C**) and FWHM (**D**).

Table S3. Effective addition rates used for the experiment shown in Figure 1A. The starting volume was 20 mL, with $[Au^0]$ = 0.25 mM. For each sample we extracted 1 mL and adjusted the effective rate ($\mu L/h$, blue column) keeping constant the *Ag added per Au mol per hour* (orange column) at a value of **0.24**.

Sample	Au^0 (mol)	V AgNO$_3$ added (mL)	Rate ($\mu L/h$)	Ag added per Au mol per hour	time (h)	AgEn
1	5.00E-06	1.50E-01	**300.0**	**0.24**	0.50	0.12
2	4.75E-06	7.13E-02	**285.2**	**0.24**	0.75	0.18
3	4.51E-06	6.76E-02	**270.6**	**0.24**	1.00	0.24
4	4.27E-06	1.28E-01	**256.0**	**0.24**	1.50	0.36
5	4.03E-06	1.21E-01	**241.6**	**0.24**	2.00	0.48
6	3.79E-06	1.14E-01	**227.5**	**0.24**	2.50	0.6
7	3.56E-06	1.07E-01	**213.5**	**0.24**	3.00	0.72
8	3.33E-06	9.99E-02	**199.8**	**0.24**	3.50	0.84
9	3.10E-06	9.31E-02	**186.2**	**0.24**	4.00	0.96
10	2.88E-06	1.73E-01	**172.8**	**0.24**	5.00	1.2
11	2.66E-06	1.60E-01	**159.8**	**0.24**	6.00	1.44
12	2.45E-06	2.94E-01	**147.0**	**0.24**	8.00	1.92
13	2.25E-06	2.70E-01	**134.9**	**0.24**	10.00	2.4
14	2.06E-06	1.73E+00	**123.4**	**0.24**	24.00	5.76
15	1.91E-06	2.75E+00	**114.7**	**0.24**	48.00	11.15

References

(1) Scarabelli, L.; Coronado-Puchau, M.; Giner-Casares, J. J.; Langer, J.; Liz-Marzán, L. M. Monodisperse Gold Nanotriangles: Size Control, Large-Scale Self-Assembly, and Performance in Surface-Enhanced Raman Scattering. *ACS Nano* **2014**, *8*, 5833–5842.

(2) Young, K. L.; Jones, M. R.; Zhang, J.; Macfarlane, R. J.; Esquivel-Sirvent, R.; Nap, R. J.; Wu, J.; Schatz, G. C.; Lee, B.; Mirkin, C. A. Assembly of Reconfigurable One-Dimensional Colloidal Superlattices due to a Synergy of Fundamental Nanoscale Forces. *Proc. Natl. Acad. Sci.* **2012**, *109*, 2240–2245.

(3) Mason, T. Osmotically Driven Shape-Dependent Colloidal Separations. *Phys. Rev. E* **2002**, *66,* 060402(R).

(4) Park, K.; Koerner, H.; Vaia, R. A. Depletion-Induced Shape and Size Selection of Gold Nanoparticles. *Nano Lett.* **2010**, *10*, 1433–1439.

(5) Mao, Y.; Cates, M. E.; Lekkerkerker, H. N. W. Depletion Force in Colloidal Systems. *Physica A* **1995**, *222*, 10–24.